THE ASTROPHYSICAL JOURNAL, 463:473–488, 1996 June 1

SPECTROSCOPY OF BRIGHT QUASARS WITH THE *HUBBLE SPACE TELESCOPE*[1] AND LYMAN-ALPHA ABSORPTION LINES IN THE REDSHIFT RANGE $0.5 < z < 1.7$

C. D. IMPEY AND C. E. PETRY
Steward Observatory, University of Arizona, Tucson, AZ 85721

AND

M. A. MALKAN AND W. WEBB
Department of Astronomy, University of California, Los Angeles, CA 90024

Received 1995 February 17; accepted 1995 December 6

ABSTRACT

We report ultraviolet spectroscopy of three bright quasars obtained with the Faint Object Spectrograph of the *Hubble Space Telescope*. The good quality spectra covering the range 1800–3300 Å result from spectropolarimetry acquired for these targets, the interpretation of which has been published elsewhere. Objective algorithms were used to select absorption lines whose strength exceeded 4 times the rms noise in the nearby continuum, resulting in 109 significant lines for PG 1222+228, 91 significant lines for PG 1634+706, and 19 significant lines for PG 2302+029. Most of the spectral range covers the region with a high density of lines due to intervening absorbers, blueward of the Lyman-α emission line.

In PG 1222+228, we identify about 35% of the lines as being associated with the seven metal line systems already known in this quasar. Three have seven or more metal lines identified. An additional 12% are either galactic lines or Lyman-α, Lyman-β pairs with no associated metals. In PG 1634+706, nearly 42% of the absorption lines are identified with metal systems. Some are associated with the two metal line systems previously known in this quasar, others are associated with two newly identified C IV systems at $z = 0.6540$ and $z = 0.9057$. Another 19% are galactic lines or Lyman-α, Lyman-β pairs with no associated metals. Six galactic lines are identified in the spectrum of PG 2302+029; no lines due to intervening absorbers could be identified.

The data for PG 1222+228 and PG 1634+706 can be used to estimate the number density of Lyman-α absorbers in the redshift range $0.5 < z < 1.7$. Above an effective rest equivalent width of 0.4 Å there are 25 Lyman-α lines in PG 1222+228 in the wavelength range 2300–3300 Å, and 11 Lyman-α lines in PG 1634+706 in the wavelength range 1865–2650 Å. We have been able to demonstrate that the identification procedure and the method of fitting lines in blended regions is unlikely to contribute systematic errors beyond the Poisson error to these numbers. The deduced number density is consistent with the number density of Lyman-α absorbers at zero redshift, using published data from the *HST* Quasar Absorption Line Key Project, indicating little or no evolution over 55% ($q_0 = 0$) to 70% ($q_0 = 0.5$) of the age of the universe. It is also consistent with an extrapolation to lower redshift of the rapid increase in number density that is seen before $z \approx 2$, implying an inflection at $z = 1$–1.5. The rapid decline in dN/dz might be caused by an ionization effect caused by the changing comoving space density of quasars, because the decline follows a similar form to the decline in the integrated UV intensity of quasars at the hydrogen Lyman edge. The evolution in dN/dz over the range $1 < z < 3$ also mirrors the change in the star formation rate in disk galaxies in the universe. It is not clear whether transition in Lyman-α evolution at $z = 1$–1.5 is due to a change in ionization state, or whether it marks a fundamental change in the intervening absorber population.

Subject headings: quasars: absorption lines — quasars: general — ultraviolet: galaxies

1. INTRODUCTION

Quasars can be used as effective probes of intervening material all the way from the local universe out to $z \approx 5$. Historically, the narrow lines in quasar spectra due to intervening absorbers have been divided into two types (Weymann, Carswell, & Smith 1981): metal lines due to extended regions around normal galaxies (Young, Sargent, & Boksenberg 1982) and intergalactic hydrogen clouds (Sargent et al. 1980). The clear distinction between these two categories may, however, be starting to blur. Recent data show that the stronger lines in the Lyman-α "forest" have detectable metals (Tytler 1995; Lu 1991), are clustered in velocity space (Chernomordik 1995; Cristiani et al. 1996), are loosely associated with galaxies at low redshift (e.g., Bahcall et al. 1993; Stocke 1995; Spinrad et al. 1993; Morris et al. 1993; Lanzetta et al. 1996) and have large physical extent (Dinshaw et al. 1995). In all these respects they bear some resemblance to the C IV and Mg II absorption systems.

Below a redshift of $z = 1.5$ the atmosphere is opaque, and Lyman-α absorption can only be studied from space. Recent results from the Quasar Absorption Line Key Project of the *Hubble Space Telescope* have begun to define the population of absorbers at low redshift (Bahcall et al. 1993; 1996). Published results on 89 Lyman-α systems with no associated metals give a local number density of lines with rest equivalent width greater than 0.32 Å of $(dN/dz)_0 \approx 19.0 \pm 4.6$. There is no evidence for cosmic evolution over the redshift range $0 < z < 1$, with $(dN/dz) \propto (1 + z)^{\gamma}$, where

[1] Based on observations with the NASA/ESA *Hubble Space Telescope*, obtained at the Space Telescope Science Institute, which is operated by the Association of Universities for Research in Astronomy, Inc., under NASA contract NAS 5-26555.

$\gamma = 0.48 \pm 0.62$. At higher redshifts, conflicting results have been published. In the range $1.5 < z < 4$ Bajtlik, Duncan & Ostriker (1988) and Lu, Wolfe, & Turnshek (1991) found rapid number density evolution with $\gamma = 2.36 \pm 0.40$ and $\gamma = 2.75 \pm 0.29$, respectively. One high-resolution echelle study produced a significantly flatter evolution, $\gamma = 1.68 \pm 0.80$ (Rauch et al. 1992). Using a homogeneous and carefully selected sample, Bechtold (1994) found $\gamma = 1.89 \pm 0.28$ for lines with rest equivalent width greater than 0.32 Å. Other large and systematic studies have been carried out by Lu (1991) and Press, Rybicki, & Schneider (1993). It is not clear whether or not evolution with a single power-law dependence can explain all available data.

This paper presents spectroscopy of three bright quasars, where objective search techniques have been used to select and identify narrow absorption lines. Several new metal line systems are discovered, in addition to ultraviolet species in existing metal line systems. The data for PG 1222+228 (Ton 1530) is used to define a new set of Lyman-α absorbers in the redshift range $0.7 < z < 1.8$. This sample is combined with existing ground and space-based samples to comment on the redshift evolution of Lyman-α absorbers over 90% of the lookback time.

2. OBSERVATIONS

Ultraviolet spectropolarimetry of PG 1222+228, PG 1634+706, and PG 2302+029 was obtained with the *Hubble Space Telescope's* (*HST*) Faint Object Spectrograph (FOS) using the 4″.3 aperture, the blue Digicon detector, and gratings G190H and G270H; the details of the observations are summarized in Table 1. Although the original motivation for obtaining these data was to obtain spectropolarimetry, the reduction process also yields high signal-to-noise spectra, which cover a wavelength range of 2000–3300 Å for PG 1222+228, 1600–3300 Å for PG 1634+706, and 2200–3300 Å for PG 2302+029. For the first two objects, the spectra include a portion of the line-rich Lyman-α "forest."

Data reduction consisted of correction of instrumental effects and calibration using standard files taken in 1991 July (with the exception of two dead diode files) that were made available by the Space Telescope Science Institute (STScI) and applied by a program written by Richard Allen of the FOS Instrument Team. A correction was made to allow for defective and dead diodes, and the data were scaled to a count rate (counts s^{-1} $pixel^{-1}$). The sky contribution was sufficiently small that sky subtraction was not required; however, a low level of instrumental background noise was subtracted. Because this background becomes a significant fraction of the continuum level for portions of the spectra, it was necessary to verify that a suitable background level was used in the reduction process.

The FOS background is primarily due to dark current in the Digicon detectors with some contribution from particle induced events. Also included in the background is a component of scattered light, probably caused by scattering off the grating. Its exact contribution cannot be determined, but it is likely to be much less than the dark current. The background is measured periodically and shows little variation, except during passage through the South Atlantic Anomaly (when no science observations are made). The validity of the standard background was tested by analyzing the values of intensity, linear polarization, and polarization angle, which were calculated after subtraction of three different levels of background from the bluest quarter of the G190H spectrum 1994–2319 Å of PG 1222+228 (G190H). These three levels were the standard value, which corresponds to a count rate of 0.0078 counts s^{-1} $pixel^{-1}$, a minimum value of zero background, and as a maximum it was assumed that all the signal in the bin, corresponding to a count rate of 0.011 counts s^{-1} $pixel^{-1}$, was background. The maximum value is likely to be too high for a background level, since there is no evidence that the dark current varies by this much during normal science observations with the FOS. It is also likely that some of the signal from 1600–1800 Å is real continuum from the quasar, as evidenced by the average intensity in the bluest quarter of the G190H spectrum of PG 1634+706, where the continuum is extinguished due to an optically thick intervening absorber, which is only 0.0025 counts s^{-1} $pixel^{-1}$. The results of the calculations showing the effects of subtracting the three different background levels on the intensity, linear polarization, and polarization angle are presented and discussed in detail in Impey et al. (1995), and confirm that the correction performed using the standard background level is appropriate.

The data were corrected for the nonuniformity of the detector response using flat fields taken with the same aperture as and closest in time to the target observations. Because it is known that the dectector response is variable with time (Jannuzi & Hartig 1994), and the flat fields were taken, in some cases, nearly a year before the data, it is possible that artificial absorption-like features could be introduced into the data due to flat-fielding, which does not accurately reflect the decreasing sensitivity of the detector. There are two circumstances under which this might occur. First, the 1991 July flats, which were used to reduce this data, have small regions that were set to unity, where strong absorption lines in the standard star used to measure the flat field occur. If the dectector sensitivity in one of these areas is lower than that of the continuum in adjacent regions, then an absorption-like residual may appear in the reduced data. The second possibility is that the detector response has declined in a particular region after the flat

TABLE 1

DETAILS OF THE OBSERVATIONS

Property	PG 1222+228	PG 1634+706	PG 2302+029
Redshift	2.046	1.334	1.044
V-magnitude	15.5	14.9	16.0
M_B[a]	−29.9	−29.6	−27.9
Date of Observation	1991 Nov 11–12	1992 Jul 23–24	1992 Jul 28
HST/FOS Gratings	G190H/G270H	G190H/G270H	G270H
Integration Times (s)	12960/14400	5280/5280	7920

[a] Luminosities calculated for $H_0 = 50$ km^{-1} Mpc^{-1}, $q_0 = 0.5$.

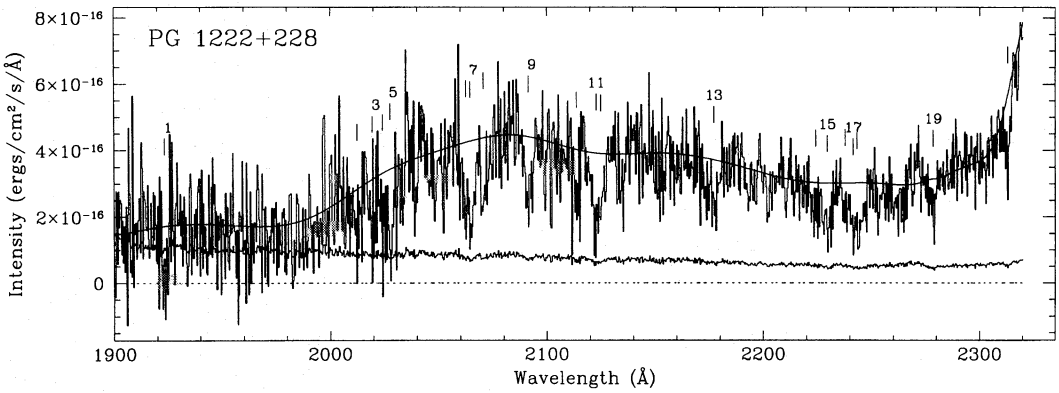

FIG. 1.—Spectrum of PG 1222+228 taken with grating G190H shown with the fitted continuum. The lower curve is the error array, and each marked line has a significance of $\geq 4\,\sigma$. Every other line is labeled and corresponds to the line number given in Table 2. Wavelengths are vacuum.

field was taken; the apparent absorption would then not be fully corrected, and an artificial absorption feature would result.

Comparison of the 1991 July flats with the next set of flats, the so-called "superflats" taken in 1993 December, can give a measure of the likelihood that these residuals could be introduced into the data and subsequently mistaken for narrow absorption lines. If the 1991 July and 1993 December flats are assumed to be a minimal and maximal correction to the data respectively (since the time of observation of the data are bracketed by these two sets of measurements), the difference of the two sets of flats is the largest likely correction that should have been made if the detector sensitivity decreased from the time of the 1991 July flat fields to the time of the data observations. Calculations show that any residual introduced as a result of either of the two situations described would have an equivalent width less than the 4 σ limiting equivalent width derived from the flux observed in each object for each grating (see Fig. 6). We conclude that the likelihood that artificial absorption-like features are introduced into the data by improper flat-fielding is low.

After flux calibration through multiplication by the inverse sensitivity function, wavelength calibration was performed. The error in the wavelength calibration was evaluated by combining in quadrature the errors introduced by

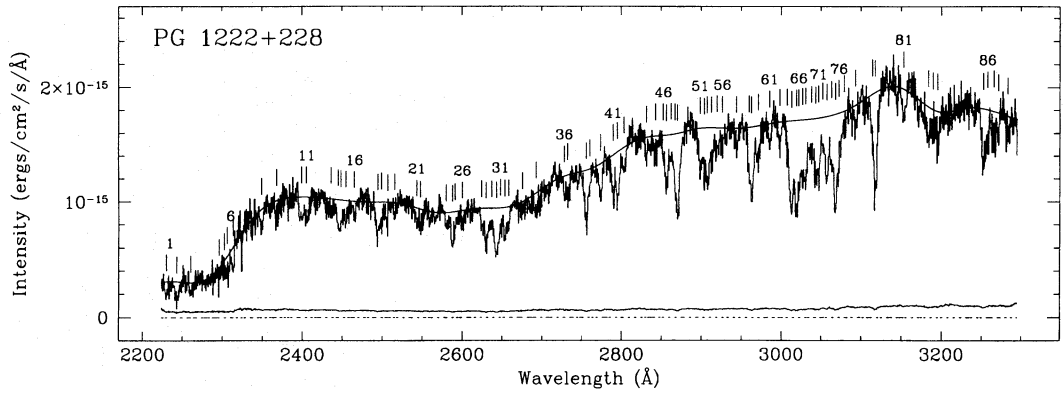

FIG. 2.—Spectrum of PG 1222+228 taken with grating G270H shown with the fitted continuum. The lower curve is the error array, and each marked line has a significance of $\geq 4\,\sigma$. Every fifth line is labeled and corresponds to the line number given in Table 3. Wavelengths are vacuum.

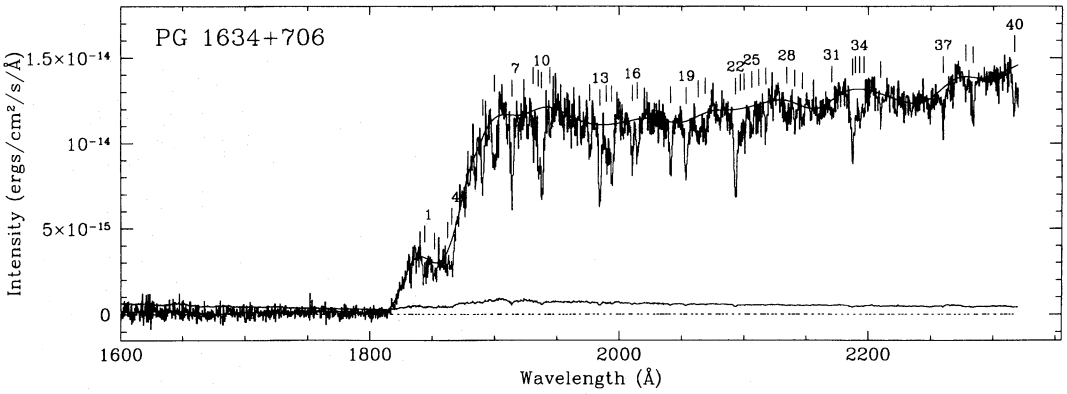

FIG. 3.—Spectrum of PG 1634+706 taken with grating G190H shown with the fitted continuum. The lower curve is the error array, and each marked line has a significance of $\geq 4\,\sigma$. Every third line is labeled and corresponds to the line number given in Table 4. Wavelengths are vacuum.

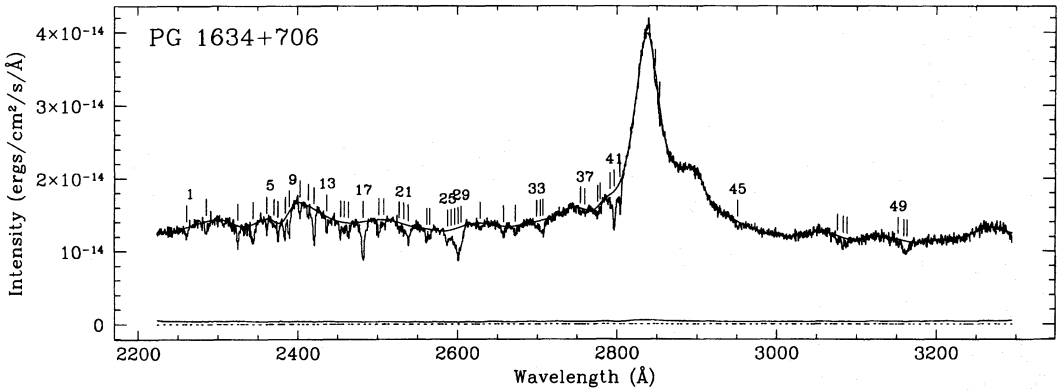

FIG. 4.—Spectrum of PG 1634+706 taken with grating G270H shown with the fitted continuum. The lower curve is the error array, and each marked line has a significance of $\geq 4\,\sigma$. Every fourth line is labeled and corresponds to the line number given in Table 5. Wavelengths are vacuum.

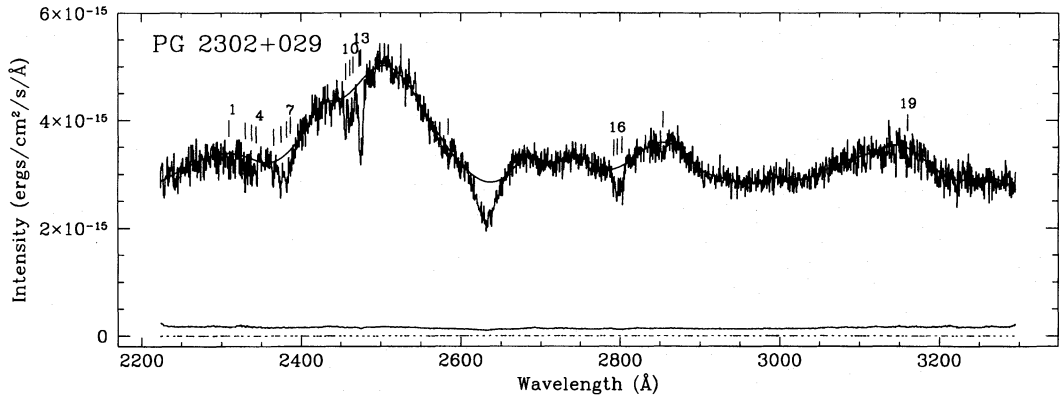

FIG. 5.—Spectrum of PG 2302+029 taken with grating G270H shown with the fitted continuum. The lower curve is the error array, and each marked line has a significance of $\geq 4\,\sigma$. Every third line is labeled and corresponds to the line number given in Table 6. Wavelengths are vacuum.

the fitted coefficients, the combination of the polarimetric *y*-steps, geomagnetic distortion, and grating jitter. The resulting rms error in the wavelength calibration is 0.58 Å for the G190H grating and 0.79 Å for the G270H grating.

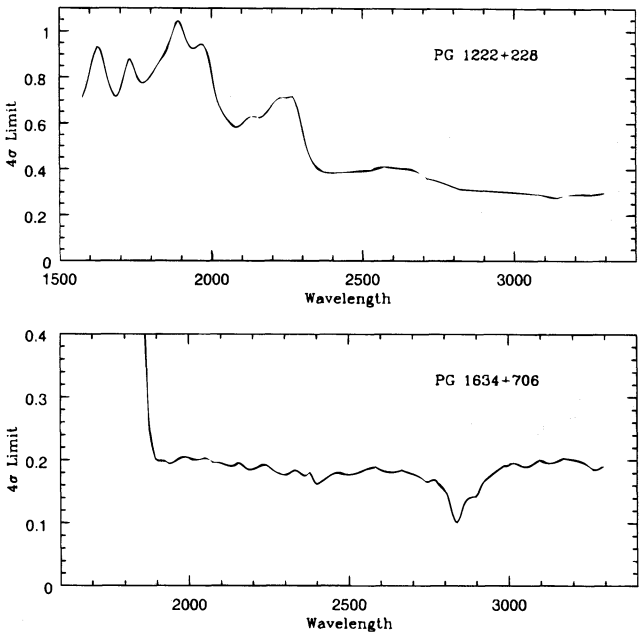

FIG. 6.—The curves shown represent the 4 σ error in the equivalent width of the lines. These errors are determined by a power-law fit to the relationship between continuum flux and measured equivalent width for lines in the spectrum of each objects. (*a*) PG 1222+228; (*b*) PG 1634+706

An explicit correction for the zero-point offset was not possible as calibration data was not obtained at the time of the observations; however, the weighted average redshift derived for ISM lines can provide a measure of the zero-point offset. The offset calculated from the redshift of the ISM lines at the midpoint of the wavelength range of the data encompasses the zero-point error quoted by the *HST* Data Handbook and is on the order of the derived error, demonstrating that a separate correction for this effect is not required.

The intensity spectra, continuum fits, and line identifications are shown in Figures 1–5, and a detailed description of the reduction and analysis of the spectropolarimetric data is presented in a separate paper (Impey et al. 1995). Here we present a spectroscopic analysis and a discussion of the line selection and identification process for these quasars.

3. ANALYSIS

3.1. *Continuum Fitting*

After instrumental corrections were completed, an interactive program written by Tom Aldcroft (Aldcroft 1993) was used to perform continuum fitting, to select and measure lines, and to view candidate redshift systems. Each continuum was determined by fitting a cubic spline to binned averages of data points. Points that deviated negatively by more than two standard deviations were flagged as possible lines, and were rejected for subsequent iterations of the fit. This process was repeated four times, although the fit was usually invariant after two or three iterations. The tightness of the fit was controlled by modifying the number of bins to be averaged. Obtaining a good fit over the entire

spectrum was difficult because of the large number of absorbers blueward of Lyman-α emission. Occasionally, it was necessary to adjust the fit parameters for small sections of the spectrum, especially in regions of heavily blended absorption lines. The resulting curve fits the broader emission profiles, and for PG 2302+029, we note a BAL feature at ~2630 Å, to which we did not attempt to fit a continuum. The procedure of iteratively rejecting discrepant points only works reliably in the case of narrow, isolated lines. While the continuum fits were generally robust to small changes in the fit parameters, we make no claim for the uniqueness of the fits in the wavelength region of the Lyman-α "forest."

3.2. *Selection of Significant Lines*

Initially, a method of optimal extraction following that described by Schneider et al. (1993) was used to detect significant lines. These lines were located in regions of the spectra that had a flux decrement 4 or more times the uncertainty in the flux measured in the adjacent continuum. For our purposes, this initial step defines significant regions which are later fitted with an assumed profile to locate and measure significant lines.

3.2.1. *The Unresolved Line Profile*

Available high-resolution data indicates that strong unblended Lyman-α absorption lines have Doppler parameters in the range 20–50 km s^{-1} (Morris et al. 1993; Rauch et al. 1993; Fan & Tytler 1994). At the resolution of the *HST* data, which corresponds to about 460 km s^{-1}, all of the lines (with the exception of strong ISM lines) can be assumed to be unresolved. Normally, a single Gaussian can be assumed to be a good approximation of a spectral line profile, but unfortunately, the line spread function (LSF) characteristic of pre-COSTAR FOS data taken with the 4″.3 aperture cannot be accurately described this simply. The FOS LSF has a broad, symmetric component that forms wings extending ±6 diodes (8.81 Å for G190H and 12.6 Å for G270H) to either side of a sharper Gaussian core. An assumed profile neglecting this component, which represents approximately 30% of the total line flux, could result in systematic effects in the line selection algorithms and equivalent width measurements. Therefore, simulations have been performed to determine what effect the use of a single Gaussian as the line profile, representing the core of the true profile and major portion of the total line flux, might have on the derived line list, the measured equivalent widths, and the subsequent calculation of dN/dz.

The FOS LSF for the 4″.3 aperture was digitized from the profile published in the FOS Instrument Handbook (Version 2.0, 1992 April) as an electronic version was unavailable. This profile was then fitted with two Gaussians, one representing the core and the other the wings, using the IRAF routine "ngaussfit," which fits multiple one-dimensional Gaussian functions and implements the least-squares fitting by a downhill simplex minimization algorithm. The ratio of the total area contributed by these two Gaussians to the area of a Gaussian fit to just the core of the profile is 1.36, which implies that about 26% of the energy in the line is contributed by the wing component.

The IRAF package "artdata" was used to simulate first a single isolated line and second a blended region having a line density of 0.10 lines $Å^{-1}$, which is typical of the Lyman-α "forest" regions of the data; five spectra were created for each case. The central wavelength of each line was randomly placed in each spectrum given the line density and creating 10 unique spectra. The amplitudes of both Gaussians were scaled so the total area of the simulated profile equals the average equivalent width of lines in the 2600 Å region of PG 1222+228, which is representative of a typical blended region of the data; all lines generated in the simulated spectra had the same equivalent width. The FWHM of the Gaussians are fixed to preserve the assumption of unresolved lines. The simulated spectra have a wavelength dispersion, continuum flux, and signal-to-noise ratio similar to that of the typical blended region.

To measure the isolated lines in the simulated spectra, the model profile is a Gaussian with FWHM equal to the best fit to the core of the digitized line spread profile. Equivalent widths are measured in two ways: directly from the best-fit Gaussian and integrating over the real data points of the line profile using the 95% limits of the best-fit Gaussian. The equivalent widths measured from the integration method will be used for single, isolated lines. For the isolated lines, the central wavelength and amplitude is varied to minimize χ^2_ν, as is done for the real data. The extracted central wavelengths are virtually identical to the input line centers. The average ratio of the input equivalent width used to generate the five simulated spectra to the integrated equivalent widths derived from the simulated spectra is 1.33 ± 0.13, which means that about 75% of the flux is recovered in measuring lines using this method. This is very close to the theoretical value that should be recovered assuming the single Gaussian is an approximation to the true line profile. This correction factor should be applied to the equivalent widths of all lines measured as single isolated lines.

For the simulation of blended regions, the spectra were fit with with multiple components given by Gaussians with FWHM equal to the best fit to the core of the digitized line spread profile. One simulated spectrum was eliminated from the sample because the random draw of line centers placed two adjacent lines within 1.5 resolution elements of one another and the line-finding software cannot distinguish between lines this close together. For blended regions it is necessary to use the equivalent width derived directly from the fitted Gaussians as they are more representative of the individual lines. The average of ratios of the input equivalent width to the measured equivalent widths for the four simulated spectra is 1.18 ± 0.06, implying that 15% of the energy in the line is missed with the single Gaussian approximation of the profile. This is closer to the true value than is obtained with the isolated line simulation, because the summed broad components of adjacent lines in a blend act to depress the adjacent continuum slightly. This correction factor should be applied to the equivalent widths measured in blended regions.

We therefore chose a Gaussian with FWHM equal to the instrumental resolution as a reasonable model of the line profile with the correction factor of 1.33 to equivalent widths of isolated lines (measured with the integration method) and 1.18 to equivalent widths of lines in blended regions (determined from the best-fit Gaussian). Due to the uncertainties of deblending lines, the second correction factor is less well determined than the first one. The instrumental resolution for the configuration used to obtain the data are determined from the FOS Instrument Handbook (Version 2.0, 1992 April), which states that the line width

(FWHM) for the 4.″3 aperture is 1.50 diodes for a point source at 3000 Å. This differs from the post-COSTAR value of 0.96 diodes. Additionally, for polarimetric data, there is a co-addition of the *y*-step data that results in a broadening of the line profile because the two spectra have some offset in wavelength that varies slightly over the wavelength range. A close look at this step in the reduction and of the fit of the wavelength calibration coefficients before and after co-addition shows that the amount of "smearing" introduced by combining the *y*-steps broadens the line profiles by about 0.5 diodes. A FWHM of 2.0 diodes for G190H, which has a dispersion of 0.3669 Å per resolution element (four resolution elements per diode), is 2.9 Å; similarly for G270H, which has a dispersion of 0.5234 Å per resolution element, 2.0 diodes corresponds to 4.2 Å. Strong ISM lines are likely to be resolved and their profiles will depart from the assumed Gaussian of instrumental resolution; therefore, equivalent widths for these lines will be in error.

3.2.2. *Fitting and Measuring Lines*

On a second pass through the data, beginning with each significant region as defined by the initial procedure, an interactive fit is performed with one or more Gaussians having the instrumental FWHM and varying the central wavelength and amplitude of each component. A result of this process is that blended regions are now considered to be consisting of adjacent lines having a difference in central wavelength of less than 2.6 times the instrumental resolution. For single, isolated lines, the best fit was determined by a minimum χ^2_ν technique. For blended regions, an iterative fit was performed with an increasing number of Gaussians. If, after a new component was added, the value of χ^2_ν decreased from the previous fit and the significance for each component of the fit was 4 σ or more, then the new set of components was accepted as the best fit. This procedure was robust in the sense that, if a region was fit with too many components, the reduced value of χ^2_ν often increased, and the significance of one or more of the individual components fell below 4 σ.

This procedure was examined for any systematic bias introduced by requiring that all lines in the multi-component fits be stronger than 4 σ. This was done by investigating how the number of lines changed by fitting the regions with an increasing number of components; the criterion for the best fit being only that the χ^2_ν for the fit either increases or falls below one. The net change in the number of lines determined by this method is less than the Poisson error; thus, any bias introduced is minimal.

The parameters for each line—the equivalent width, the central wavelength, and their uncertainties—were then calculated using two methods: Gaussian fitting and integration. The first derives the parameters directly from the best-fit Gaussian profile, and the second fixes the continuum at the 95% limits of the fitted Gaussian and integrates over the spectral data. For the second method, the central wavelength is a weighted mean over the line profile.

The method used to obtain the measurements recorded for each line in the final lists is dependent on whether the line was isolated or was part of a blended region. For isolated lines, the values calculated using the integration method were used. This method gives a better estimate of the parameters for lines that are not affected by the close presence of neighboring lines because no presumptions about the shape of line profiles are made, but it is inadequate if the lines are blended. Consequently, for blended regions, the line parameters were calculated from the multiple component Gaussian fit, as it is the best model of the individual, unresolved lines. Because the lines are selected on the basis of the significance calculated from the Gaussian fit, lines ultimately measured with the integration technique may report a lower significance than is calculated from the Gaussian method.

Lists presenting all significant lines are given in Tables 2–6 for each object and each grating; vacuum wavelengths are quoted in all cases. Lines reporting parameters calculated using the integration technique have a χ^2_ν that is unique from those of adjacent lines, where adjacent lines fit as components of a blend have identical χ^2_ν-values. The equivalent widths reported in the tables are systematic underestimates, due to the presence of broad shallow wings in the unresolved line profile. To recover the total equivalent width, they must be scaled by a factor of 1.33 for isolated lines and 1.18 for lines in blended regions. In Tables 2–6 about 77% of the lines are in blends.

3.3. *Line Identification*

The identification of absorption lines presents a challenging problem, especially in the Lyman-α "forest" regions. Initially, heavy element redshift systems established in previous work (Sargent, Boksenberg, & Steidel 1988; Bechtold et al. 1984; Steidel & Sargent 1992; Kinney et al. 1991) for each object were used to identify lines selected using the procedure described above. Subsequently, searches are performed for new redshift systems that have associated metals and for systems that consist only of Lyman-α, β pairs.

3.3.1. *Confirming Known Redshift Systems*

We rederived the redshift of each previously published system for each object using the following procedure. A search list was compiled, which consisted of 52 strong lines taken from Morton, York, & Jenkins (1988). Significant lines in the spectra were identified with a published redshift system if the wavelength difference between a redshifted comparison line and an observed line was less than or equal to the instrumental resolution: 2.9 Å FWHM for the G190H grating and 4.2 Å FWHM for the G270H grating. The redshifts of each system were redetermined by taking the average of redshifts calculated from the observed and comparison line wavelengths of strong lines belonging to that system. This average was weighted by the variance of the line strength (variance weighting was used because the line strength errors are not exactly normally distributed; weighting by the rms produces a negligible difference of 0.0001–0.0002 in the redshifts). The new values of redshift, their rms error, and the number of lines on which the calculation was based are listed along with the published redshifts in Tables 7 and 8. The rms error in redshift due to wavelength calibration is 0.0003, which encompasses the mean redshift determined for galactic lines (we identify three galactic absorptions lines in PG 1222+228, seven in PG 1634+706, and six in PG 2302+029). Therefore, the uncertainties in the redshifts of the metal line systems are dominated by internal errors.

A test was performed to confirm the use of the instrumental resolution as the wavelength window to identify lines for rederivation of published redshift systems and to establish a window with which to identify weaker members of these systems. We selected PG 1634+706 for this evaluation

TABLE 2

LINE IDENTIFICATION FOR PG 1222+228 (G190H)

Line	λ_{vac} (Å)	Equivalent Width[a] (Å)	Significance	χ^2_ν	Redshift	Identification	Residual (Å)
1.....	1923.43 ± 0.61	2.27 ± 0.87	2.6	1.14	...	...	...
2.....	2012.56 ± 0.37	1.79 ± 0.37	4.9	2.02	0.6682	Si III λ1206	0.075
3.....	2019.61 ± 0.33	1.82 ± 0.33	5.5	2.02	...	...	...
4.....	2024.51 ± 0.30	2.08 ± 0.31	6.8	2.02	...	...	...
5.....	2028.20 ± 0.25	2.29 ± 0.29	8.0	2.02	0.6682	H I λ1215	−0.268
6.....	2061.80 ± 0.32	1.53 ± 0.25	6.2	1.32	...	...	...
7.....	2065.09 ± 0.24	1.98 ± 0.23	8.5	1.32	0.6682	N V λ1238	1.462
8.....	2070.56 ± 0.25	1.59 ± 0.22	7.3	1.32	...	...	...
9.....	2091.55 ± 0.20	1.59 ± 0.22	7.2	0.69	...	...	...
10.....	2113.43 ± 0.26	1.26 ± 0.23	5.5	2.99	1.3070	N II λ915	−1.159
11.....	2122.26 ± 0.25	1.94 ± 0.23	8.4	0.79	...	...	...
12.....	2125.30 ± 0.41	1.19 ± 0.25	4.9	0.79	...	...	...
13.....	2177.46 ± 0.23	1.31 ± 0.22	6.1	1.78	...	...	...
14.....	2224.41 ± 0.29	1.27 ± 0.21	6.0	1.64	...	...	...
15.....	2229.89 ± 0.20	1.76 ± 0.19	9.2	1.64	1.1738	H I λ1025	−0.220
16.....	2238.03 ± 0.43	0.94 ± 0.22	4.3	1.24	1.1828	H I λ1025	0.930
17.....	2241.99 ± 0.28	1.64 ± 0.21	7.7	1.24	1.3070	O I λ971	−0.239
18.....	2245.24 ± 0.28	1.49 ± 0.21	7.0	1.24	...	...	...
19.....	2278.40 ± 0.34	0.90 ± 0.20	4.4	1.19	...	...	...
20.....	2313.07 ± 0.21	1.01 ± 0.14	7.5	1.54	...	...	...

[a] Due to the broad wings of the large science aperture LSF, these equivalent widths are a measurement of the core of the profile; to recover the total equivalent width, they must be scaled by a factor of 1.33 for isolated lines and 1.18 for lines in blended regions.

because of its relatively smooth continuum and large number of strong, isolated absorption lines.

Examination of the residuals for the G190H grating using the published redshift values shows that 19 lines were found to lie within 2.9 Å of the redshifted comparison lines. Of these 19 lines, 68% fell within 1.5 Å of the predicted central wavelength and 54% of these were within 0.5 Å. Two lines that were lying outside 1.5 Å are double identifications. For the G270H grating, using a window of 4.2 Å, 69% of the 32 selected lines had residuals of less than 2.0 Å, and five lines outside 2.5 Å were double identifications. Of the lines that fell within 2.0 Å of the predicted wavelength center, 64% were within 1.0 Å. This indicates that the instrumental resolution window can reliably identify strong isolated lines associated with the published absorption systems, which are subseqently used to rederive the redshift.

An appropriate range in which a line must fall to be considered a member of the sytem is established by using the redetermined values of redshift and starting with a window of width equal to instrumental FWHM. For a match range of 2.9 Å for the G190H grating, 69% of the 26 selected lines, including all of the strong, isolated lines, had residuals of less than 1.5 Å, or 2.6 times the uncertainty in the wavelength calibration for this grating. 61% of these lines had residuals of less than 0.5 Å, and two lines with residuals more than 2.0 Å were double identifications. This implies more lines lie closer to the predicted wavelengths using redetermined redshift values than in the case where the published redshift values are used—as is expected. In order to maximize the number of potentially correct identifications and minimize the number of false identifications, we chose the range in which a line is considered a match to be 1.5 Å for grating G190H.

Similarly, for the G270H grating, using the redetermined redshifts and a match region of 4.2 Å, 80% of the 35 selected absorption lines, including all of the strong, isolated lines, had residuals less than 2.0 Å, or 2.5 times the uncertainty in the wavelength calibration for this grating. Of these lines, 79% fell within 1.0 Å of the predicted wavelength center. Three lines having residuals more than 2.5 Å are double identifications. Here again, a tighter scatter about the predicted wavelength calculated with the redetermined redshift is observed, and consequently, a wavelength range for an acceptable match range of 2.0 Å was chosen for grating G270H.

The set of redetermined values of redshift and the ranges chosen to define an acceptable match (1.5 Å for G190H and 2.0 Å for G270H) were then used in the procedure to identify lines in the observed line lists for all objects and gratings. The search algorithm is described as follows: for each object and for each redshift system, the lines from the comparison list were redshifted, and significant lines falling within the defined range for the grating were considered to be tentative identifications and were recorded in the list. In the event of multiple identifications of the same line, it was required that the correct identification be a line both closer in wavelength and stronger in oscillator strength (Morton et al. 1988) than any other candidate identification. If one line was closer and the other was stronger, both identifications are listed in the table, with the weaker line relegated to a footnote. Using these criteria, no line had more than two possible identifications.

Line strengths were not used to evaluate membership of a system except in the case of Lyman lines. Lyman-α, when it falls within the wavelength range of the data, must be the strongest member of the system ($z = 1.3070$ for PG 1222+228 is the one exception to this rule). Higher order Lyman lines are judged by the following criteria for inclusion in known redshift systems. If the equivalent width of a component of the series decreases significantly with increasing order, the line is accepted as a member of the series. If a member of the series is missing, and its predicted strength is less than the 4 σ rms of the adjacent continuum, all remaining higher order lines that might be identified on the basis of their wavelength are discounted as members of the series. If the predicted strength (based on lower order members or

TABLE 3

LINE IDENTIFICATION FOR PG 1222+228 (G270H)

Line	λ_{vac} (Å)	Equivalent Width[a] (Å)	Significance	χ^2_ν	Redshift	Identification	Residual (Å)
1.....	2229.80 ± 0.47	1.47 ± 0.33	4.4	1.06	1.1738	H I λ1025	−0.130
2.....	2243.42 ± 0.24	2.61 ± 0.29	9.1	1.39	...	...	...
3.....	2261.43 ± 0.51	1.22 ± 0.29	4.1	1.16	...	...	...
4.....	2296.18 ± 0.46	1.24 ± 0.21	5.8	1.94	...	...	...
5.....	2302.99 ± 0.60	1.02 ± 0.21	4.8	1.94	...	...	...
6.....	2307.54 ± 0.45	1.33 ± 0.20	6.8	1.94	...	...	...
7.....	2313.49 ± 0.36	1.26 ± 0.16	7.7	1.94	...	...	...
8.....	2349.44 ± 0.45	0.69 ± 0.14	4.9	0.63	...	...	...
9.....	2368.44 ± 0.41	0.61 ± 0.12	4.9	1.73	1.5238	H I λ937	−1.564
10.....	2399.31 ± 0.27	1.00 ± 0.11	9.3	1.32	...	...	...
11.....	2406.23 ± 0.27	1.01 ± 0.11	9.5	1.32	...	...	...
12.....	2436.51 ± 0.44	0.66 ± 0.12	5.7	1.32	1.5650	H I λ949	−0.454
13.....	2445.25 ± 0.42	1.03 ± 0.16	6.4	1.32	...	...	...
14.....	2449.00 ± 0.54	0.84 ± 0.16	5.4	1.32	...	...	...
15.....	2454.79 ± 0.35	0.84 ± 0.11	8.0	1.32	1.5238	H I λ972	−0.253
16.....	2465.63 ± 0.45	0.60 ± 0.10	5.8	1.32	1.5238	C III λ977	0.237
17.....	2494.07 ± 0.21	1.37 ± 0.10	13.8	1.47	1.5650	H I λ972	0.487
18.....	2499.15 ± 0.32	0.93 ± 0.10	9.0	1.47	1.3070	N II λ1083[b]	1.561
19.....	2505.85 ± 0.32	0.83 ± 0.10	8.4	1.47	...	...	...
20.....	2515.59 ± 0.58	0.37 ± 0.11	3.4	0.95	...	...	...
21.....	2543.59 ± 0.46	0.63 ± 0.11	6.0	1.41	...	...	...
22.....	2548.84 ± 0.38	0.77 ± 0.10	7.3	1.41	1.4857	H I λ1025	0.808
23.....	2581.35 ± 0.40	0.67 ± 0.10	6.5	1.10	0.6682	C IV λ1548	1.299
24.....	2588.16 ± 0.19	1.50 ± 0.10	15.4	1.10	1.5238	H I λ1025	0.609
25.....	2593.44 ± 0.56	0.51 ± 0.11	4.8	1.10	1.5272	H I λ1025	−1.194
26.....	2600.69 ± 0.38	0.67 ± 0.10	6.7	1.10	0.0002	Fe II λ2600	−0.127
27.....	2625.37 ± 0.34	0.80 ± 0.10	8.0	1.02	...	...	...
28.....	2630.71 ± 0.16	1.70 ± 0.09	18.6	1.02	1.5650	H I λ1025	0.231
29.....	2636.54 ± 0.33	0.84 ± 0.10	8.6	1.02	...	...	...
30.....	2642.57 ± 0.16	1.97 ± 0.10	19.1	1.02	1.1738	H I λ1215	0.000
31.....	2646.98 ± 0.26	1.26 ± 0.11	11.0	1.02	...	...	...
32.....	2653.58 ± 0.28	1.17 ± 0.11	10.8	1.02	1.1828	H I λ1215	0.000
33.....	2658.11 ± 0.42	0.74 ± 0.11	6.8	1.02	...	...	...
34.....	2676.44 ± 0.34	0.60 ± 0.10	5.8	1.57	...	...	...
35.....	2693.17 ± 0.29	0.85 ± 0.12	7.3	2.10	1.4857	N II λ1083	1.315
36.....	2728.93 ± 0.53	0.58 ± 0.10	5.6	0.97	1.9809	N II λ915	0.427
37.....	2733.53 ± 0.39	0.74 ± 0.10	7.3	0.97	...	...	...
38.....	2755.74 ± 0.15	1.74 ± 0.09	19.0	1.41	...	...	...
39.....	2759.96 ± 0.53	0.53 ± 0.10	5.4	1.41	...	...	...
40.....	2773.90 ± 0.17	1.00 ± 0.08	12.1	1.02	...	...	...
41.....	2789.96 ± 0.18	1.25 ± 0.08	15.4	1.26	...	...	...
42.....	2795.66 ± 0.14	1.44 ± 0.08	18.7	1.26	...	...	...
43.....	2803.33 ± 0.29	0.70 ± 0.08	8.9	1.26	1.3070	H I λ1215[c]	1.160
44.....	2831.82 ± 0.38	0.46 ± 0.08	5.4	1.31	1.9809	H I λ949	−0.722
45.....	2842.69 ± 0.38	0.43 ± 0.08	5.3	1.33	...	...	...
46.....	2852.68 ± 0.69	0.43 ± 0.11	4.0	1.13	0.0002	Mg II λ2853	0.712
47.....	2856.67 ± 0.25	1.28 ± 0.10	13.2	1.13	1.9376	H I λ972	0.254
48.....	2862.09 ± 0.41	0.62 ± 0.08	7.5	1.13	...	...	...
49.....	2867.50 ± 0.24	1.34 ± 0.10	13.2	1.13	1.3070	N V λ1242	−0.413
50.....	2871.27 ± 0.16	1.77 ± 0.10	17.3	1.13	1.9376	C III λ977	−1.158
51.....	2898.65 ± 0.24	0.98 ± 0.08	12.1	1.37	1.9809	H I λ972	0.395
52.....	2903.51 ± 0.34	0.88 ± 0.09	10.2	1.37	1.9376	O I λ988	0.601
53.....	2908.00 ± 0.22	1.31 ± 0.08	15.7	1.37	1.3070	Si II λ1260	−0.269
54.....	2913.15 ± 0.26	0.89 ± 0.08	11.3	1.37	1.9809	C III λ977	−0.723
55.....	2919.41 ± 0.33	0.63 ± 0.08	8.1	1.37	...	...	...
56.....	2925.79 ± 0.46	0.45 ± 0.08	5.7	1.37	...	...	...
57.....	2943.95 ± 0.42	0.44 ± 0.09	5.1	0.95	...	...	...
58.....	2960.03 ± 0.28	1.04 ± 0.10	10.0	1.45	1.4857	Si II λ1190	−1.001
59.....	2963.84 ± 0.18	1.56 ± 0.10	15.5	1.45	...	...	...
60.....	2970.86 ± 0.21	0.92 ± 0.08	12.0	1.45	...	...	...
61.....	2985.40 ± 0.38	0.43 ± 0.08	5.2	0.78	1.4857	N I λ1200	−1.993
62.....	2998.27 ± 0.34	0.48 ± 0.08	5.9	0.81	1.4857	Si III λ1206	0.739
63.....	3009.15 ± 0.32	0.90 ± 0.10	8.6	1.26	1.3070	Si II λ1304	−0.031
64.....	3013.07 ± 0.15	2.04 ± 0.09	22.4	1.26	1.9376	H I λ1025	0.092
65.....	3018.34 ± 0.18	1.93 ± 0.10	18.5	1.26	2.0535	O I λ988	0.389
66.....	3022.17 ± 0.26	1.50 ± 0.10	14.5	1.26	1.4857	H I λ1215a[d]	−0.367
67.....	3026.77 ± 0.29	1.26 ± 0.09	13.4	1.26	...	...	...
68.....	3030.98 ± 0.22	1.37 ± 0.10	14.3	1.26	1.9376	O VI λ1031	0.407
69.....	3036.80 ± 0.26	0.86 ± 0.08	10.7	1.26	...	...	...
70.....	3042.57 ± 0.19	1.36 ± 0.08	16.4	1.26	1.9376	C II λ1036	1.772

TABLE 3—*Continued*

Line	λ_{vac} (Å)	Equivalent Width[a] Å	Significance	χ^2_ν	Redshift	Identification	Residual (Å)
71.....	3047.18 ± 0.20	1.34 ± 0.08	16.1	1.26	1.9376	O VI λ1037	0.919
72.....	3052.74 ± 0.46	0.63 ± 0.09	6.7	1.26	...	...	...
73.....	3057.43 ± 0.19	1.48 ± 0.09	17.1	1.26	1.9809	H I λ1025	0.156
74.....	3062.98 ± 0.24	1.13 ± 0.09	12.9	1.26	...	...	...
75.....	3067.90 ± 0.15	2.06 ± 0.08	24.6	1.26	1.5238	H I λ1215	0.269
76.....	3072.29 ± 0.25	1.14 ± 0.09	12.8	1.26	1.5272	H I λ1215	0.000
77.....	3077.83 ± 0.52	0.46 ± 0.09	5.1	1.26	1.9809	O VI λ1031[e]	−1.750
78.....	3092.62 ± 0.39	0.45 ± 0.09	5.1	0.99	1.9809	O VI λ1037	0.418
79.....	3114.11 ± 0.33	0.83 ± 0.10	8.5	1.86	...	...	...
80.....	3118.15 ± 0.12	2.08 ± 0.09	23.6	1.86	1.5650	H I λ1215	0.000
81.....	3153.07 ± 0.32	0.63 ± 0.10	6.6	0.48	...	...	...
82.....	3183.38 ± 0.28	0.80 ± 0.09	9.3	1.44	1.9376	N II λ1083	0.949
83.....	3189.46 ± 0.45	0.55 ± 0.09	6.0	1.44	...	...	...
84.....	3195.68 ± 0.30	0.81 ± 0.09	8.8	1.44	...	...	...
85.....	3252.20 ± 0.19	1.30 ± 0.09	14.6	1.32	...	...	...
86.....	3257.32 ± 0.33	0.80 ± 0.10	8.2	1.32	...	...	...
87.....	3265.10 ± 0.35	0.80 ± 0.11	7.5	1.32	...	...	...
88.....	3270.18 ± 0.58	0.50 ± 0.11	4.7	1.32	...	...	...
89.....	3283.25 ± 0.45	0.45 ± 0.10	4.4	1.07	...	...	...

[a] Due to the broad wings of the large science aperture LSF, these equivalent widths are a measurement of the core of the profile; to recover the total equivalent width, they must be scaled by a factor of 1.33 for isolated lines and 1.18 for lines in blended regions.

[b] Also identified at $z = 1.5238$ as N III λ989 with residual −1.069.

[c] Also identified at $z = 0.0002$ as Mg II λ2803 with residual 0.621.

[d] Also identified at $z = 2.0535$ as N III λ989 with residual 0.193.

[e] Also identified at $z = 1.3070$ as C II λ1334 with residual 0.869.

other published values) is more than the 4 σ rms of the adjacent continuum, the equivalent width of the next member of the series must decrease significantly to be identified as part of the series.

The final line identifications resulting from the previously established redshift systems are listed in Tables 2–6, where the last column gives the wavelength residual, in the sense $\lambda_{pred} - \lambda_{obs}$, where the predicted wavelength is calculated using the redetermined redshift for each system.

3.3.2. *Searching for New Redshift Systems*

After having identified as many lines as possible using published redshift systems, a search was made for new systems. By stepping through the spectrum by a redshift increment equal to that of the instrumental resolution, the number of matches between the observed line list and the comparison line list can be determined at each redshift. It might be expected that the number of matches would peak strongly at the previously established redshift system values, and also at any new redshift systems. However, due to the relatively short wavelength range of the spectrum and the high number of random matches, no such signal was seen. A similar attempt at correlation was made using the sum of the significances of the lines found to match at a particular value of redshift instead of the number of lines. But this method also failed to indicate the known redshift systems and therefore was not a reliable indicator of new redshift systems.

Ultimately, a method similar to that used by Bahcall et al. (1993) was adopted whereby each unidentified, significant line for both gratings of an object was considered in turn to be Lyman-α, its redshift was calculated, and the line list was searched for higher order Lyman lines and metal lines in that candidate system. Searching only as yet unidentified significant lines, insures that the strongest lines that will define the system are unambiguously identified. Because searching for new systems (with our software) requires looking for lines from both gratings (which have different resolutions) simultaneously, only one range defining an acceptable match is needed. Therefore, the lines were considered to be associated with a new system if they gave a wavelength match within the specified range for the G190H grating (1.5 Å), since in the test case for the G270H grating (2.0 Å), over 96% of the identified, strong lines in the known systems had residuals of less than 1.5 Å.

The following criteria were used to judge the reliability of a proposed redshift system, in order of importance, where the line strengths are those expected based on oscillator strengths published by Morton et al. (1988): (1) Lyman-α must be the strongest line in the system (if it is within the range of the spectrum); (2) if Lyman-β is predicted to fall within the wavelength range of the spectrum, it must be present with strength less than that of Lyman-α; (3) either the C IV λλ1548/1550 doublet or the O VI λλ1031/1037 doublet must be present; (4) if the C IV doublet is present, C IV λ1548 must be stronger than C IV λ1550; (5) if the O VI doublet is present, O VI λ1037 must be stronger than O VI λ1031; (6) if the S IV doublet is present, S IV λ1393 must be stronger than Si IV λ1402; (7) any of C II λ1334, O I λ1302, Si II λ1260, C II λ1036, O I λ988, or C II λ977 may be present, these being the strongest lines from the Morton list; (8) higher order lines beyond Lyman-β may be present.

Lines fulfilling the above criteria were used to redetermine the redshift and to search for other weaker or blended members using the complete list of significant lines. The criteria applied for accepting a line as an identification and for handling double identifications were the same as those used for the previously published systems. These lines are recorded in Tables 2–6 with their wavelength residuals. Redshifts that identified Lyman-α, β pairs, but had no associated metal lines, are also listed in the tables noting the redshift determined from the Lyman-α line. All new and existing metal line systems are listed in Tables 7 and 8.

TABLE 4

LINE IDENTIFICATION FOR PG 1634+706 (G190H)

Line	λ_{vac} (Å)	Equivalent Width[a] (Å)	Significance	χ^2_ν	Redshift	Identification	Residual (Å)
1.....	1844.06 ± 0.22	1.23 ± 0.18	6.9	1.49	...	...	...
2.....	1852.23 ± 0.31	0.94 ± 0.19	5.0	1.09	...	...	...
3.....	1862.10 ± 0.36	0.83 ± 0.15	5.4	0.86	0.9057	C III λ977	−0.182
4.....	1865.95 ± 0.19	1.38 ± 0.13	10.4	0.86	...	...	...
5.....	1890.21 ± 0.24	0.54 ± 0.09	5.9	1.28	...	...	...
6.....	1899.55 ± 0.17	0.88 ± 0.10	9.2	1.05	...	...	...
7.....	1913.71 ± 0.12	1.01 ± 0.08	12.8	1.31	...	...	...
8.....	1931.21 ± 0.41	0.38 ± 0.08	4.7	1.36	...	...	...
9.....	1935.27 ± 0.25	0.79 ± 0.09	9.1	1.36	...	...	...
10.....	1938.21 ± 0.13	1.26 ± 0.08	15.5	1.36	...	...	...
11.....	1944.33 ± 0.38	0.36 ± 0.07	4.8	1.36	0.9907	C III λ977	0.646
12.....	1975.92 ± 0.40	0.30 ± 0.08	3.7	1.18	0.9057	O VI λ1037	1.464
13.....	1984.51 ± 0.10	1.23 ± 0.06	19.2	1.21	1.0407	H I λ972	0.136
14.....	1990.00 ± 0.24	0.60 ± 0.08	8.0	1.21	...	...	...
15.....	1994.01 ± 0.15	0.95 ± 0.07	13.1	1.21	1.0407	C III λ977	−0.203
16.....	2010.15 ± 0.20	0.63 ± 0.07	9.5	0.98	0.6540	H I λ1215	0.568
17.....	2014.58 ± 0.22	0.55 ± 0.07	8.3	0.98	...	...	...
18.....	2041.10 ± 0.16	0.60 ± 0.07	8.9	0.82	0.9907	H I λ1025	0.816
19.....	2053.45 ± 0.12	0.85 ± 0.07	12.8	0.90	0.9907	O VI λ1031	0.816
20.....	2063.28 ± 0.25	0.43 ± 0.06	7.0	0.92	0.9907	C II λ1036	−0.234
21.....	2068.90 ± 0.28	0.38 ± 0.06	6.3	0.92	1.0183	H I λ1025	1.318
22.....	2093.01 ± 0.08	1.35 ± 0.05	26.8	1.35	1.0407	H I λ1025	0.171
23.....	2096.75 ± 0.29	0.44 ± 0.06	7.3	1.35	...	...	...
24.....	2100.37 ± 0.28	0.42 ± 0.06	7.1	1.35	...	...	...
25.....	2106.15 ± 0.23	0.43 ± 0.06	7.8	1.35	1.0407	O VI λ1031	−0.308
26.....	2112.09 ± 0.36	0.27 ± 0.06	4.8	1.35	1.0580	H I λ1025	−1.195
27.....	2117.40 ± 0.25	0.38 ± 0.05	7.2	1.35	1.0407	O VI λ1037	0.052
28.....	2134.37 ± 0.26	0.36 ± 0.05	7.0	1.13	...	...	...
29.....	2140.94 ± 0.34	0.28 ± 0.05	5.3	1.13	1.0885	H I λ1025	1.317
30.....	2146.93 ± 0.43	0.22 ± 0.05	4.1	1.13	...	...	...
31.....	2170.32 ± 0.44	0.20 ± 0.06	3.5	0.80	...	...	...
32.....	2187.00 ± 0.15	0.88 ± 0.07	12.7	1.70	...	...	...
33.....	2189.62 ± 0.49	0.33 ± 0.07	5.1	1.70	...	...	...
34.....	2192.97 ± 0.31	0.42 ± 0.05	8.0	1.70	...	...	...
35.....	2196.20 ± 0.37	0.29 ± 0.05	5.5	1.70	...	...	...
36.....	2209.56 ± 0.28	0.27 ± 0.05	5.4	1.16	...	...	...
37.....	2259.76 ± 0.16	0.42 ± 0.05	8.9	1.19	...	...	...
38.....	2277.71 ± 0.37	0.19 ± 0.04	4.7	1.07	1.2201	H I λ1025	−0.554
39.....	2283.52 ± 0.13	0.55 ± 0.04	14.4	1.07	1.2275	H I λ1025	1.230
40.....	2316.82 ± 0.11	0.56 ± 0.04	14.0	1.82	0.9057	H I λ1215	−0.118

[a] Due to the broad wings of the large science aperture LSF, these equivalent widths are a measurement of the core of the profile; to recover the total equivalent width, they must be scaled by a factor of 1.33 for isolated lines and 1.18 for lines in blended regions.

3.4. *Individual Heavy Element Absorption Systems*

3.4.1. *PG 1634+706* ($z_{abs} = 0.6694$)

Lines associated with this system, published by Steidel & Sargent (1992), are not apparent in our data. There is no evidence for an absorption line at the predicted location of Lyman-α for this system. The C IV doublet is predicted to be in a blended region whose components are otherwise identified. The stronger component of the Si IV doublet is not within selection range of any lines and the predicted location of the weaker component is in competition with a galactic Fe II line.

3.4.2. *PG 1634+706* ($z_{abs} = 0.6540 \pm 0.0005$)

A new absorption system is found for this quasar by identifying line 16 from Table 4 as Lyman-α and the C IV doublet (λλ1548, 1550) as lines 23 and 24 from Table 5. Line 16 is the strongest of the three and line 23 is stronger than line 24 as is predicted by Morton et al. (1988) for these C IV lines. Lyman-β, higher order Lyman lines, and the O VI doublet (λλ1031, 1037) are not shifted into the observed window for this spectrum. The components of the Si IV doublet (λλ1393, 1402) have expected strengths on the order of the rms of the spectral region where they should appear; they are not detected as significant lines. However, a close inspection of both gratings of this object in the wavelength region where Si IV is expected to appear reveals weak features that may be identified as the Si IV doublet. Similarly, the metal lines that are likely to be found in the range of this spectrum (i.e., C II λ1334, O I λ1302, and Si II λ1260) are too weak to be detected as significant lines.

3.4.3. *PG 1634+706* ($z_{abs} = 0.9057 \pm 0.0004$)

A second new absorption system is found by identifying line 40 in Table 4 as Lyman-α. Five other previously unidentified lines are associated with this redshift system, of which line 40 is the strongest. (Lyman-α is also seen, somewhat more weakly, in the G270H spectrum). Lyman-β falls within the range of the spectrum, but it is not detected because its expected strength is on the order of the rms for the region where it should appear. Both the O VI doublet and the C IV doublet can be seen in the spectrum, but only the stronger components are identified as significant lines—line 12 from Table 4 and line 45 from Table 5. The weaker

TABLE 5

LINE IDENTIFICATION FOR PG 1634+706 (G270H)

Line	λ_{vac} (Å)	Equivalent Width[a] (Å)	Significance	χ^2_ν	Redshift	Identification	Residual (Å)
1.....	2260.80 ± 0.34	0.39 ± 0.06	6.3	0.73	...	...	...
2.....	2285.78 ± 0.27	0.49 ± 0.06	8.1	1.24	1.2275	H I λ1025	−1.030
3.....	2325.21 ± 0.19	0.65 ± 0.06	10.5	1.88	...	...	...
4.....	2343.89 ± 0.12	0.87 ± 0.05	16.2	1.77	0.0003	Fe II λ2344	0.910
5.....	2360.80 ± 0.41	0.27 ± 0.05	5.3	1.87	0.9057	N V λ1238	0.021
6.....	2369.40 ± 0.65	0.20 ± 0.05	4.0	1.26	0.9907	Si II λ1190	0.373
7.....	2375.28 ± 0.28	0.50 ± 0.05	9.9	1.26	0.9907	Si II λ1193	0.214
8.....	2383.39 ± 0.20	0.65 ± 0.05	13.6	1.98	0.0003	Fe II λ2382	−0.029
9.....	2389.17 ± 0.14	0.82 ± 0.04	19.1	1.98	0.9907	N I λ1200	0.126
10.....	2403.05 ± 0.31	0.29 ± 0.04	6.4	2.08	0.9907	Si III λ1206[b]	−1.258
11.....	2413.37 ± 0.31	0.35 ± 0.04	8.4	2.16	...	...	...
12.....	2420.36 ± 0.09	1.17 ± 0.04	30.1	2.16	0.9907	H I λ1215	−0.313
13.....	2436.77 ± 0.21	0.50 ± 0.05	10.0	1.58	1.0407	Si II λ1193	−1.635
14.....	2453.59 ± 0.24	0.56 ± 0.05	12.1	1.75	1.0183	H I λ1215	0.000
15.....	2458.55 ± 0.48	0.30 ± 0.05	6.3	1.75	...	...	...
16.....	2463.98 ± 0.24	0.52 ± 0.04	11.7	1.75	1.0407	Si III λ1206	−1.887
17.....	2482.21 ± 0.05	1.61 ± 0.04	40.2	1.67	1.0407	H I λ1215	−1.404
18.....	2501.80 ± 0.18	0.60 ± 0.04	14.8	1.75	1.0580	H I λ1215	0.000
19.....	2508.62 ± 0.41	0.26 ± 0.04	6.2	1.75	0.9907	Si II λ1260	0.515
20.....	2527.64 ± 0.37	0.31 ± 0.04	7.2	1.29	1.0407	N V λ1238	0.410
21.....	2533.44 ± 0.33	0.37 ± 0.04	8.5	1.29	...	...	...
22.....	2538.97 ± 0.15	0.78 ± 0.04	19.0	1.29	1.0885	H I λ1215	0.000
23.....	2561.23 ± 0.30	0.47 ± 0.05	9.5	1.34	0.6540	C IV λ1548	−0.504
24.....	2565.62 ± 0.42	0.33 ± 0.05	6.7	1.34	0.6540	C IV λ1550	−0.640
25.....	2587.04 ± 0.23	0.61 ± 0.05	12.5	1.35	0.0003	Fe II λ2586	0.257
26.....	2591.65 ± 0.44	0.40 ± 0.05	8.0	1.35	0.9907	O I λ1302	0.590
27.....	2596.31 ± 0.26	0.69 ± 0.05	14.0	1.35	0.9907	Si II λ1304	0.314
28.....	2600.85 ± 0.13	1.36 ± 0.05	29.3	1.35	0.0003	Fe II λ2600	−0.027
29.....	2605.25 ± 0.17	0.82 ± 0.05	17.2	1.35	...	...	...
30.....	2628.82 ± 0.29	0.29 ± 0.04	6.8	1.25	...	...	...
31.....	2657.57 ± 0.21	0.45 ± 0.04	10.1	1.36	0.9907	C II λ1334[c]	−0.903
32.....	2672.70 ± 0.23	0.41 ± 0.04	9.3	1.08	0.9057	Si IV λ1402	0.559
33.....	2698.85 ± 0.52	0.26 ± 0.05	5.3	1.30	1.2201	H I λ1215	0.000
34.....	2704.17 ± 0.57	0.35 ± 0.06	5.5	1.30	...	...	...
35.....	2707.85 ± 0.31	0.56 ± 0.07	8.5	1.30	1.2275	H I λ1215	0.000
36.....	2754.09 ± 0.49	0.21 ± 0.04	5.4	0.72	...	...	...
37.....	2760.09 ± 0.65	0.16 ± 0.04	4.1	0.72	...	...	...
38.....	2775.19 ± 0.41	0.33 ± 0.05	6.7	1.62	0.9907	Si IV λ1393	−0.628
39.....	2779.27 ± 0.82	0.17 ± 0.05	3.4	1.62	...	...	...
40.....	2791.45 ± 0.32	0.34 ± 0.04	8.7	2.20	0.9907	Si IV λ1402	1.058
41.....	2796.63 ± 0.08	1.26 ± 0.03	36.5	2.20	0.0003	Mg II λ2796	0.421
42.....	2803.60 ± 0.11	0.80 ± 0.03	24.6	2.20	0.0003	Mg II λ2803	0.632
43.....	2847.56 ± 0.45	0.16 ± 0.03	5.9	1.14	...	...	...
44.....	2853.28 ± 0.31	0.25 ± 0.03	8.7	1.14	0.0003	Mg I λ2853	0.397
45.....	2951.02 ± 0.36	0.28 ± 0.05	5.9	0.99	0.9057	C IV λ1548	−0.611
46.....	3075.94 ± 0.48	0.28 ± 0.05	5.2	1.36	...	...	...
47.....	3082.82 ± 0.37	0.45 ± 0.06	7.5	1.36	0.9907	C IV λ1548	−0.799
48.....	3087.63 ± 0.49	0.33 ± 0.06	5.7	1.36	0.9907	C IV λ1550	−0.489
49.....	3151.72 ± 0.57	0.26 ± 0.06	4.4	1.17	...	...	...
50.....	3159.41 ± 0.29	0.63 ± 0.06	10.0	1.17	1.0407	C IV λ1548	−0.010
51.....	3163.76 ± 0.34	0.55 ± 0.07	8.3	1.17	1.0407	C IV λ1550	0.889

[a] Due to the broad wings of the large science aperture LSF, these equivalent widths are a measurement of the core of the profile; to recover the total equivalent width, they must be scaled by a factor of 1.33 for isolated lines and 1.18 for lines in blended regions.

[b] Also identified at $z = 0.9057$ as Si II λ1260 Å with residual −1.063.

[c] Also identified at $z = 1.0407$ as O I λ1302 Å with residual −0.248.

components, O VI λ1031 and C IV λ1550, can be discerned as features of less than 4 σ significance at the predicted location and expected strengths for these doublets. Line 32 from Table 5 is uniquely identified as Si IV λ1402, the weaker component of the doublet. The stronger component, Si IV λ1393, lies within 1.5 Å of Line 31 from Table 5 and is most likely blended with lines from two other absorption systems, which are both closer and stronger. The remaining metal lines except Si II λ1260, which shares an identification with line 5, are blended with lines identified with other absorption systems. All higher order Lyman lines are too weak to be detected due to the Lyman limits of the strong $z = 0.9907$ and $z = 1.0407$ systems.

3.4.4. *PG 2302+029*

The quasar PG 2302+029 is clearly worthy of further study. Although we could identify no narrow intervening absorption lines, and none have been identified by previous workers, the spectrum shows a notable BAL feature longward of Lyman-α. Wampler (1986) found strong Fe II emission, with a total flux of 6×10^{46} ergs s^{-1}. The quasar has optical and ultraviolet polarization of ~1%, and appears to

TABLE 6

LINE IDENTIFICATION FOR PG 2302+029 (G270H)

Line	λ_{vac} (Å)	Equivalent Width[a] (Å)	Significance	χ^2_ν	Redshift	Identification	Residual (Å)
1.....	2309.75 ± 0.56	0.36 ± 0.09	3.9	1.20	...	...	...
2.....	2329.81 ± 0.47	0.55 ± 0.10	5.7	1.66	...	...	...
3.....	2337.32 ± 0.56	0.43 ± 0.09	4.7	1.66	...	...	...
4.....	2343.67 ± 0.56	0.42 ± 0.09	4.7	1.66	0.0002	Fe II λ2344	0.896
5.....	2365.27 ± 0.54	0.39 ± 0.08	4.7	0.95	...	...	...
6.....	2374.23 ± 0.27	0.79 ± 0.08	9.7	0.95	0.0002	Fe II λ2374	0.587
7.....	2381.47 ± 0.25	0.90 ± 0.08	11.1	0.95	0.0002	Fe II λ2382	1.653
8.....	2387.17 ± 0.50	0.43 ± 0.08	5.3	0.95	...	...	...
9.....	2455.62 ± 0.29	0.61 ± 0.06	9.5	1.60	...	...	...
10.....	2461.23 ± 0.39	0.56 ± 0.07	8.0	1.60	...	...	...
11.....	2465.82 ± 0.50	0.41 ± 0.07	5.8	1.60	...	...	...
12.....	2473.66 ± 0.31	0.98 ± 0.13	7.3	1.60	...	...	...
13.....	2476.76 ± 0.31	0.98 ± 0.13	7.3	1.60	...	...	...
14.....	2583.78 ± 0.69	0.24 ± 0.07	3.3	1.21	...	...	...
15.....	2791.77 ± 0.47	0.48 ± 0.08	6.0	1.19	...	...	...
16.....	2796.64 ± 0.27	0.79 ± 0.08	10.6	1.19	0.0002	Mg II λ2796	0.132
17.....	2802.75 ± 0.25	0.73 ± 0.07	10.7	1.19	0.0002	Mg II λ2803	1.201
18.....	2854.07 ± 0.43	0.33 ± 0.07	4.7	1.29	0.0002	Mg I λ2853	−0.678
19.....	3159.43 ± 0.54	0.34 ± 0.09	3.9	1.48	...	...	...

[a] Due to the broad wings of the large science aperture LSF, these equivalent widths are a measurement of the core of the profile; to recover the total equivalent width, they must be scaled by a factor of 1.33 for isolated lines and 1.18 for lines in blended regions.

be variable (see discussion in Impey et al. 1995). PG 2302+029, therefore, appears to be one of the rare and interesting class of quasars where obscuring or scattering material is seen in both the emission line outflow and the polarization.

3.5. *Lyman-α Absorption Systems*

The primary goal of this analysis is the identification of a set of Lyman-α absorbers at intermediate redshift. The two bright quasars, PG 1634+706 at $z_{em} = 1.334$ and PG 1222+228 at $z_{em} = 2.046$ offer the prospect of defining dN/dz in a gap between the redshift range covered by the published observations of Quasar Key Project and the redshift range that can be accessed from the ground. The most obvious evidence that the spectra of both quasars have a significant number of intervening hydrogen systems is the strong excess of narrow absorption lines seen shortward of Lyman-α emission (see Fig. 4 for PG 1634+706 and Bechtold et al. 1984 for PG 1222+228). When the quasars and the absorbers are at low redshift ($z < 0.5$), the absorption line density is low and metal line systems are rare, so line identification is relatively straightforward. When the quasars and the absorbers are at high redshifts ($z > 2$), the line density is high and blending can be severe. To preserve a reliable Lyman-α line list, lines shortward of the Lyman-β emission wavelength are not usually considered (Lu et al. 1991; Bechtold 1994). In our case, the Lyman-α line density is too low to obtain a meaningful result if the wavelength range is truncated at the Lyman-β emission wavelength. Consequently, we must carefully consider the issues of blending, contamination by metal lines, and confusion with higher order Lyman series lines.

TABLE 7

ABSORPTION SYSTEMS FOR PG 1222+228

Redshift (z)	Number of Lines	Published z	Reference
0.6682 ± 0.0013.....	5	0.6681	1
1.3070 ± 0.0013.....	8	1.3070	2
1.4857 ± 0.0007.....	6	1.4867	1
1.5238 ± 0.0016.....	6	1.5239	1
1.9376 ± 0.0010.....	8	1.9372	1
1.9809 ± 0.0006.....	7	1.9805	1
2.0535 ± 0.0019.....	2	2.0555	1

REFERENCES.—(1) Sargent et al. 1988; (2) Bechtold et al. 1984.

TABLE 8

ABSORPTION SYSTEMS FOR PG 1634+706

Redshift (z)	Number of Lines	Published z	Reference
0.6540 ± 0.0005.....	3	...	1
	...	0.6694	2
0.9057 ± 0.0004.....	7	...	1
0.9907 ± 0.0006.....	17	0.9903	2
1.0407 ± 0.0007.....	12	1.046	3

REFERENCES.—(1) This paper; (2) Steidel & Sargent 1992; (3) Kinney et al. 1991.

3.5.1. *Contamination by Heavy Element Systems*

The procedure for identifying metal line systems has already been discussed. All lines that are identified, according to the previously described procedure, with a heavy element species within the wavelength search window are then removed from future consideration. Because PG 1228+228 and PG 1634+706 are fairly well-studied and most of their previously published metal line systems were derived from optical data, the likelihood that associated metal lines remain to be identified in the Lyman-α "forest" is low. However, for PG 2302+029, no optical data is available and any metal line systems have yet to be discovered, making its Lyman-α "forest" suspect as to the presence of associated metal lines that could be mistaken for Lyman-α lines. We did not explore the possibility of weak or rare species beyond the search list of Morton et al. (1988). Given the expected Lyman-α line density and the relative strengths of the adopted metal lines, it is unlikely that any Lyman-α lines have been falsely identified as metals. Equally, it is

unlikely that we have overcounted Lyman-α lines by missing weak or rare metal line transitions.

3.5.2. *Higher Order Lyman Lines*

Higher order Lyman lines associated with the metal systems have been identified using the criteria described for inclusion of these lines described in § 3.3.1. We identified Lyman-γ in three metal systems and Lyman-δ for two metal systems in PG 1222+228, and Lyman-γ for one metal system in PG 1634+706. The likelihood that we have undercounted Lyman-α lines by falsely identifying them as hydrogen lines from a heavy element system is low.

Lyman-α, β pairs that have no associated metal lines have been detected with the procedure described in § 3.3.2 and are listed along with the other line identifications in Tables 2–6 with the redshift calculated from the Lyman-α line.

3.5.3. *Effects of Line Blending*

Limited resolution and signal-to-noise can combine with a high line density to make the reliable identification of individual lines very difficult. The effects of line blending are clearly seen in the Lyman-α "forest" region of PG 1222+228 (Figs. 1 and 2). It is not obvious *a priori* how blending will affect a line list that is selected to some fixed equivalent width limit. Therefore, we experimented with multicomponent fitting of Gaussian profiles to blended regions, to see how robust the final line list might be to changes in the fitting procedure.

The procedure involved each region that was fit by two or more components in the original data reduction. In a complex region, the number of components was increased until the reduced value of χ^2_ν stopped decreasing. In the test procedure, we deliberately underfitted or overfitted the region by one component. In each case, the rest equivalent width of each component is derived assuming it is a Lyman-α line. Then we observe how the number of components above a threshold of 0.32 Å rest equivalent width changes as the fit is varied (of course, due to the omission of broad line wings, the true equivalent width threshold is somewhat higher, about 0.4 Å rest equivalent width). The experiment was performed on PG 1222+228 because it has the most severe blending. We fitted 15 complexes in the region 2300–3260 Å. The number of components per complex was in the range 2–7, with a total of 56 components. The results were that in 75% (16/21) cases, incrementing the fit by one component did not change the final line list. Underfitting was equally likely to add or subtract components to the final list, the average change was 0 ± 1.2 components. Overfitting was more likely to reduce the number of components that made the final list, by an average of -1.5 ± 1.6 components.

These tests are not exhaustive, but they allow us to estimate the effect of fitting multiple components to blended regions on the final Lyman-α line list. Statistically, overfitting reduces the final number of lines by $-1.5(15/4) \approx 6$ out of 56. However, only $\frac{1}{4}$ of the lines in this wavelength region are expected to be Lyman-α, so the effect of overfitting is to lose 1–2 Lyman-α lines. Since this is less then the Poisson error in the number of Lyman-α lines in this wavelength region, we conclude that our fitting procedure is unlikely to significantly bias our estimate of dN/dz.

3.5.4. *The Calculation of dN/dz*

Starting with the line lists in Tables 3–6, we cull out metal lines, Lyman lines associated with metal line systems, and Lyman-β lines associated with strong Lyman-α. The high end of the wavelength range is set either by $(z_{em} - 0.15)$ or the red end of the G270H data to avoid the proximity effect (Bechtold 1994). The blue end of the wavelength range is set by the point at which the 4 σ noise in the spectrum rises above the adopted rest frame equivalent width limit of 0.32 Å (appropriate to the line cores). The included wavelength and redshift ranges are 2300–3300 Å, $z = 0.89$–1.71 for PG 1222+228, and 1865–2650 Å, $z = 0.53$–1.18 for PG 1634+706. Then only lines detected at 4 σ or better significance are selected. The result is 25 Lyman-α lines in PG 1222+228 and 11 Lyman-α lines in PG 1634+706; final lines lists are given in Tables 9 and 10. To convert to dN/dz, we must account for the fact that the detected lines reflect a higher rest equivalent width limit than 0.32 Å, because this refers only to the line cores. In PG 1222+228, the effective equivalent width limit is 0.38 Å; in PG 1634+706, the effec-

TABLE 9

LYMAN-α LINES FOR PG 1222+228

Line[a]	λ_{vac}	Equivalent Width	Significance (Å)	Redshift (Å)
5.....	2302.99 ± 0.60	1.02 ± 0.21	4.8	0.8944
6.....	2307.54 ± 0.45	1.33 ± 0.20	6.8	0.8982
7.....	2313.49 ± 0.36	1.26 ± 0.16	7.7	0.9031
10.....	2399.31 ± 0.27	1.00 ± 0.11	9.3	0.9737
11.....	2406.23 ± 0.27	1.01 ± 0.11	9.5	0.9793
13.....	2445.25 ± 0.42	1.03 ± 0.16	6.4	1.0114
14.....	2449.00 ± 0.54	0.84 ± 0.16	5.4	1.0145
19.....	2505.85 ± 0.32	0.83 ± 0.10	8.4	1.0613
27.....	2625.37 ± 0.34	0.80 ± 0.10	8.0	1.1596
29.....	2636.54 ± 0.33	0.84 ± 0.10	8.6	1.1688
30.....	2642.57 ± 0.16	1.97 ± 0.10	19.1	1.1738
31.....	2646.98 ± 0.26	1.26 ± 0.11	11.0	1.1774
32.....	2653.58 ± 0.28	1.17 ± 0.11	10.8	1.1828
33.....	2658.11 ± 0.42	0.74 ± 0.11	6.8	1.1865
38.....	2755.74 ± 0.15	1.74 ± 0.09	19.0	1.2668
40.....	2773.90 ± 0.17	1.00 ± 0.08	12.1	1.2818
42.....	2795.66 ± 0.14	1.44 ± 0.08	18.7	1.2999
59.....	2963.84 ± 0.18	1.56 ± 0.10	15.5	1.4380
67.....	3026.77 ± 0.29	1.26 ± 0.09	13.4	1.4898
69.....	3036.80 ± 0.26	0.86 ± 0.08	10.7	1.4980
74.....	3062.98 ± 0.24	1.13 ± 0.09	12.9	1.5196
76.....	3072.29 ± 0.25	1.14 ± 0.09	12.8	1.5272
79.....	3114.11 ± 0.33	0.83 ± 0.10	8.5	1.5616
80.....	3118.15 ± 0.12	2.08 ± 0.09	23.6	1.5650
85.....	3252.20 ± 0.19	1.30 ± 0.09	14.6	1.6752

[a] Line numbers correspond to the G270H grating.

TABLE 10

LYMAN-α LINES FOR PG 1634+706

Line[a]	λ_{vac}	Equivalent Width	Significance (Å)	Redshift (Å)
4.....	1865.95 ± 0.19	1.38 ± 0.13	10.4	0.5349
6.....	1899.55 ± 0.17	0.88 ± 0.10	9.2	0.5626
7.....	1913.71 ± 0.12	1.01 ± 0.08	12.8	0.5742
9.....	1935.27 ± 0.25	0.79 ± 0.09	9.1	0.5919
10.....	1938.21 ± 0.13	1.26 ± 0.08	15.5	0.5944
14.....	1990.00 ± 0.24	0.60 ± 0.08	8.0	0.6370
17.....	2014.58 ± 0.22	0.55 ± 0.07	8.3	0.6572
32.....	2187.00 ± 0.15	0.88 ± 0.07	12.7	0.7990
3[b].....	2325.21 ± 0.19	0.65 ± 0.06	10.5	0.9127
22[b].....	2538.97 ± 0.15	0.78 ± 0.04	19.0	1.0885
29[b].....	2605.25 ± 0.17	0.82 ± 0.05	17.2	1.1431

[a] Line numbers correspond to the G190H grating.
[b] Line number corresponds to the G270H grating.

tive equivalent width limit is 0.39 Å. Taking an exponential scaling with rest equivalent width and normalizing to 0.21 Å, increased the line densities by a factor of 1.34 for PG 1222+228 and 1.40 for PG 1634+706. This yields log $(dN/dz) = 1.61^{+0.08}_{-0.09}$ at log $(1 + z) = 0.35 \pm 0.08$ for PG 1222+228, and log $(dN/dz) = 1.38^{+0.11}_{-0.16}$ at log $(1 + z) = 0.26 \pm 0.08$ for PG 1634+706.

Another datum can be included based on the observations of the quasar pair Q0107−025A and B by Dinshaw et al. (1995). There are 10 Lyman-α lines in the two lines of sight, four of which are in common to the two lines of sight within a velocity difference of 150 km s^{-1}. The wavelength and redshift range is 1800–2300 Å and $z = 0.48$–0.89, using only lines stronger than a rest equivalent width of 0.33 Å. It is difficult to justify using the full set of 10 lines from both lines of sight, since the geometry of the absorbers is unknown, and so the contingent probability of observing a given Lyman-α line in two closely separated lines of sight cannot be determined. Therefore, we count only seven lines over the redshift range, since seven lines are observed in *each* object. The result for Q0107−025 yields log $(dN/dz) = 1.23^{+0.14}_{-0.21}$ at log $(1 + z) = 0.23 \pm 0.05$, in excellent agreement with log (dN/dz) for PG 1634+706. These data points are added to the published Quasar Absorption line Key Project results (Bahcall et al. 1993) and ground-based results beyond $z = 1.6$ (Bechtold 1994) in Figure 7. Although other larger datasets are available for comparison (e.g., Lu 1991), we prefer to compare to the compilation of Bechtold 1994 for the simple reason that the line selection was carried out with the same software.

These new estimates of dN/dz agree well with published data, and with recent measurements from the Key Project (Bahcall et al. 1996). Within the errors, the two new points in Figure 7 (and the data point from Dinshaw et al. 1995) are consistent *both* with an extrapolation of the published Key Project data with no evolution back to $z = 1$–1.5, and with an extrapolation to lower redshifts of the evolution with $\gamma = 1.89$ seen for high-redshift data. The error bars are still too large for a firm conclusion, but there are indications of a change in the behavior of dN/dz at $z = 1$–1.5.

4. DISCUSSION

The main result of this paper is to put a new constraint on the number density evolution of Lyman-α absorbers at intermediate redshifts. We use 36 hydrogen lines in the spectra of two quasars observed with the *HST* to define dN/dz in the range $0.5 < z < 1.7$. The data span the gap between the results of the published observations of the Quasars Absorption Line Key project and various ground-based studies, an interval of one third of the lookback time. Since some very basic properties—size, geometry, clustering, degree of ionization, and metal content—are poorly determined, we make only brief comments on the evolution and physical properties of the absorbers.

It is still uncertain whether or not the entire population of Lyman-α absorbers from $z = 0$–4 can be described by a power-law function, $dN/dz \propto (1 + z)^{\gamma}$, with a single value of γ. Formally, $\gamma = 1.26 \pm 0.13$ provides an acceptable fit to published data (Bechtold 1994), and this is also true when the data described here are included. The strongest deviation from a power-law fit to the ground-based data occurs at low redshift. Figure 8 shows a version of the number density evolution in terms of lookback time, for a critical density universe with $H_0 = 100$ km s^{-1} Mpc^{-1}. Our new measurements are consistent with an extrapolation of the Key Project data (Bahcall et al. 1993), indicating no evolution over two thirds of the lookback time. The lowest redshift point is essentially defined by only three quasars; recent Key Project results (Bahcall et al. 1996) will define the low-redshift behavior with more accuracy. Beyond $z \approx 1.5$ there is a rapid rise by a factor of 3 in dN/dz. At the highest redshifts measured to date, there is suggestive evidence of a flattening of the evolution (Bechtold 1994; Lu et al. 1991). New samples of high-redshift quasars will allow the Lyman-α absorbers to be studied up to $z \approx 5$

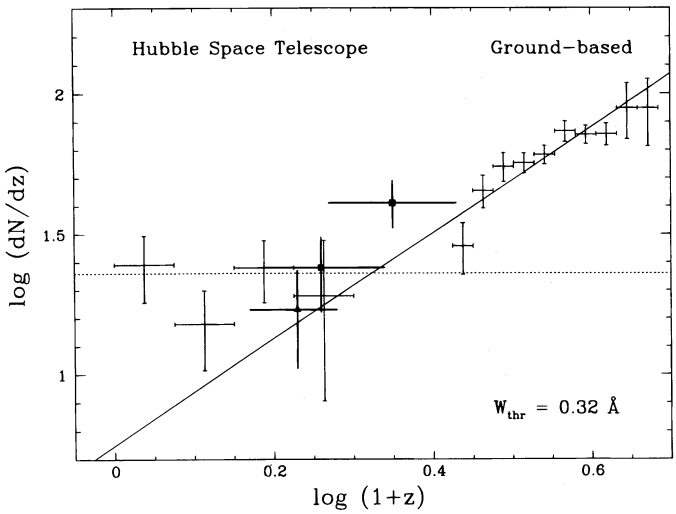

FIG. 7.—Evolution in the number density of Lyman-α absorbers from $z = 0$–3.7. Data from this paper are denoted by the large square symbols, triangle gives data point from Dinshaw et al. (1995). Low-redshift data is from the *HST* Absorption Line Key Project (Bahcall et al. 1993), high-redshift data is from Bechtold (1994). Dashed line is a no-evolution fit to the Key Project data. Solid line is a fit to the data of Bechtold using $\gamma = 1.89$.

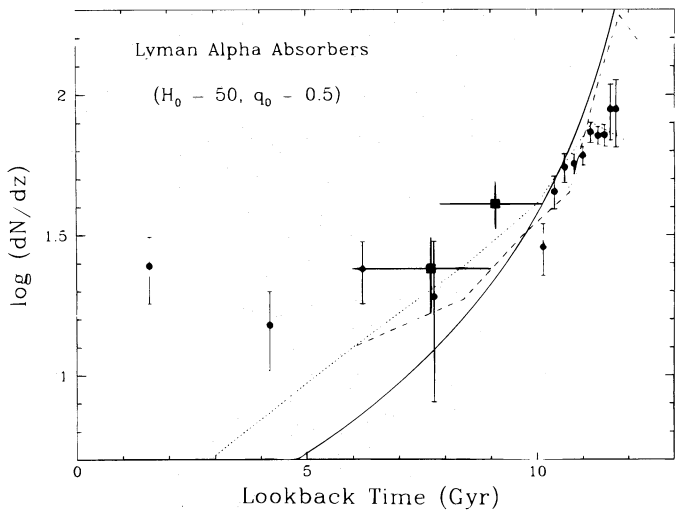

FIG. 8.—Evolution in the number density of Lyman-α absorbers as a function of cosmic time, using the same data as in Fig. 7. The solid line is the log of the comoving density for a freely expanding Hubble sphere. The dotted line is the log of the intensity of the ultraviolet background integrated over redshift from Madau (1992). The dashed line is the log of the star formation rate per Gyr for disk galaxies from the model of Wyse (1993). The zero point of all three curves is arbitrary.

(Schneider, Schmidt, & Gunn 1991; Irwin, McMahon, & Hazard 1991). Blending and metal line contamination will make interpretation of the spectra formidably difficult, although statistical techniques have been developed for the analysis (Press et al. 1993).

If the evolutionary behavior of Lyman-α absorbers changed 8–9 Gyr ago, it will be difficult to interpret without better knowledge of the physical properties of the absorbers. For example, the transition could be due to an ionization change associated with the clouds becoming more neutral, or it could mark a fundamental change in the intervening absorber population (but see Weymann 1993 for cautionary remarks on the nature of absorber "populations"). Superimposed on the absorber number density evolution, Figure 8 shows three relevant aspects of the high-redshift universe. The solid line shows the evolution in density of either a smoothly distributed component of the IGM or a freely expanding Hubble sphere, $\rho \propto (1 + z)^3$. The dotted line shows the *log* of the intensity of the diffuse radiation field at the Lyman edge as a function of redshift (Madau 1992). Although the comoving space density of quasars, taken from Schmidt, Schneider, & Gunn (1991), shows a strong peak at $z = 2$–2.5, the volume integral over redshift shows a more gradual decline with decreasing redshift. The dashed line shows a theoretical estimate of star formation rate per Gyr in disk galaxies, assuming it is proportional to the rate at which substructure turns around and collapses (Wyse 1993). The star formation rate peaks at $z = 3$–4 and diminishes thereafter, but a smaller amount of disk formation continues to later epochs. This theoretical expectation is in accordance with the results of *N*-body simulations (Evrard, Summers, & Davis 1994) and with the observed evolution of galaxies (Colless et al. 1993; Lilly 1993; Treyer & Silk 1994). All three curves in Figure 8 have an arbitrary normalization.

First, we note that Lyman-α absorbers appear to be associated with bright galaxies at low redshift (e.g., Bahcall et al. 1991; Stocke 1995; Spinrad et al. 1993; Morris et al. 1993; Lanzetta et al. 1996). The local absorbers are not randomly distributed, but they are not as strongly clustered as luminous galaxies. More speculatively, we might associate higher redshift absorbers ($0.5 < z < 1.5$) with the blue, star-forming galaxies seen in deep CCD surveys; both populations are weakly clustered (Cristiani et al. 1996; Efstathiou et al. 1991). Figure 8 shows also that the number density of Lyman-α absorbers falls off at the approximately the same rate as the disk galaxy formation rate over the range $0.5 < z < 3$. In this scenario, we might identify Lyman-α absorbers with the tidal debris in small groups of galaxies (Morris & van den Bergh 1994).

A second observation to be made from Figure 8 is that the most rapid change in the space density of absorbers occurs around the epoch of quasar formation. It should be noted that there is some dispute about the falloff in quasar space density at high redshifts. Irwin et al. (1991) claim that there is no evidence for a decline in the space density of the most luminous quasars, but see Schneider et al. (1991) for a counter view. This issue affects the normalization of the radiation intensity, but does not strongly affect the shape of the falloff below $z = 2.5$. The decline in the number density of Lyman-α absorbers might be explained in principle as an ionization effect. There might be a single population of absorbers, but their detectability would be affected by a rapid change in the ambient ultraviolet flux density after the population of quasars peaks in the range $z = 2$–3. As others have speculated, the subsequent flattening of dN/dz at low redshifts might be associated with the transition from pressure-confined clouds to gravitationally confined clouds.

Finally, we note that a realistic interpretation of Lyman-α absorbers is likely to involve gravitationally and hydrodynamical processes and a complex geometry. Cen et al. (1994) have proposed that the absorbers are confined by a combination of gravity and ram pressure from infalling gas. In their simulations, the low column density clouds have sheet-like or filamentary geometry, and the absorption arises in shock-heated regions that resemble Zel'dovich pancakes. The implication is that Lyman-α absorbers join galaxies as legitimate probes of the formation of structure from primordial density fluctuations in the universe. The models of Cen et al. (1994) predict evolution in dN/dz with $\gamma \approx 2.2$ in the range $2 < z < 3$, in reasonable accord with observations although the H I column densities may be too high. Also, recent observations of quasars pairs show a large size for the absorbers, at least 100 kpc in extent at $z > 1$ (Dinshaw et al. 1995), which is consistent with models where the absorbers have low dimensionality. Also, when we combine *HST* and ground-based observations of quasar pairs (Dinshaw et al. 1994), the characteristic size of the absorbers increases from 70 kpc at $z = 1.9$ to 350 kpc at $z = 0.7$. This mimics free Hubble expansion and is suggestive of the post-shock evolution of filamentary clouds in the models of Cen et al. (1994). The evolution of Lyman-α absorbers can now be studied over 90% of the age of the universe, with important implications for the evolution of large-scale structure.

We are grateful to Tom Aldcroft for the use of his absorption line measuring software and for assistance in its proper use. We thank the referee, Buell Jannuzi, for his diligent efforts to improve the clarity of this paper. We acknowledge useful conversations with Jill Bechtold, Nadine Dinshaw and Craig Foltz. This work was supported by NASA through GO Program grant numbers 2524 and 3732 from the Space Telescope Science Institute, which is operated by the Association of Universities for Research in Astronomy, Inc, under NASA contract NAS 5-26555.

REFERENCES

Aldcroft, T. 1993, Ph.D. thesis, Stanford Univ.
Bahcall, J. N., Jannuzi, B. T., Schneider, D. P., Hartig, G. F., Bohlin, R., & Junkkarinen, V. 1991, ApJ, 377, L5
Bahcall, J. N., et al. 1993, ApJS, 87, 1
Bahcall, J. N., et al. 1996, ApJ, 457, 19
Bajtlik, S., Duncan, R. C., & Ostriker, J. P. 1988, ApJ, 327, 570
Bechtold, J. 1994, ApJS, 91, 1
Bechtold, J., et al. 1984, ApJ, 281, 76
Bechtold, J., Crotts, A. P. S., Duncan, R. C., & Fang, Y. 1994, ApJ, 437, L83
Cen, R., Miralda-Escude, J., Ostriker, J. P., & Rauch, M. 1994, ApJ, 437, L9
Chernomordik, V. 1995, ApJ, 440, 431
Cristiani, S., D'Odorico, S., Fontana, A., Giallongo, E., & Savaglio, S. 1996, ApJ, in press
Colless, M., Ellis, R., Broadhurst, T., Taylor, K., & Peterson, B. 1993, MNRAS, 261, 19
Dinshaw, N., Foltz, C. B., Impey, C. D., Weymann, R. J., & Morris, S. L. 1995, Nature, 373, 223
Dinshaw, N., Impey, C. D., Foltz, C. B., Weymann, R. J., & Chaffee, F. C. 1994, ApJ, 437, L87
Efstathiou, G., Bernstein, G., Katz, N., Tyson, J. A., & Guhathakurta, P. 1991, ApJ, 380, 47
Evrard, A. E., Summers, F. J., & Davis, M. 1994, ApJ, 422, 11
Fan, X.-M., & Tytler, D. 1994, ApJS, 94, 17

Impey, C. D., Malkan, M. A., Webb, W., & Petry, C. E. 1995, ApJ, 440, 80
Irwin, M. J., McMahon, R. G., & Hazard, C. H. 1991, in ASP Conf. Ser. 21, The Space Distribution of Quasars, ed. D. Crampton (San Francisco: ASP), 117
Jannuzi, B. T., & Hartig, G. F. 1994, in Proc. Workshop on Calibrating *Hubble Space Telescope*, ed. C. J. Blades & S. Osmer (Baltimore: STScI), 215
Kinney, A. L., Bohlin, R. C., Blades, J. C., & York, D. G. 1991, ApJS, 75, 645
Lanzetta, K., et al. 1996, ApJ, in press
Lilly, S. J. 1993, ApJ, 411, 501
Lu, L. 1991, ApJ, 379, 99
Lu, L., Wolfe, A. M., & Turnshek, D. A. 1991, ApJ, 367, 19
Madau, P. 1992, ApJ, 389, L1
Morris, S. L., & van den Bergh, S. 1994, ApJ, 427, 696
Morris, S. L., Weymann, R. J., Dressler, A., McCarthy, P. J., Smith, B. A., Terrile, R. J., Giovanelli, R., & Irwin, M. J. 1993, ApJ, 419, 524
Morton, D. C., York, D. G., & Jenkins, E. B. 1988, ApJS, 68, 449
Press, W. H., Rybicki, G. B., & Schneider, D. P. 1993, ApJ, 414, 64
Rauch, M., Carswell, R. F., Chaffee, F. H., Foltz, C. B., Webb, J. K., Weymann, R. J., Bechtold, J., & Green, R. F. 1992, ApJ, 390, 387
Rauch, M., Carswell, R. F., Webb, J. K., & Weymann, R. J. 1993, MNRAS, 260, 468
Sargent, W. L. W., Boksenberg, A., & Steidel, C. C. 1988, ApJS, 68, 539
Sargent, W. L. W., Young, P. J., Boksenberg, A., & Tytler, D. 1980, ApJS, 42, 41
Schmidt, M., Schneider, D. P., & Gunn, J. E. 1991, in ASP Conf. Ser. 21, The Space Distribution of Quasars, ed. D. Crampton (San Francisco: ASP), 109
Schneider, D. P., Schmidt, M., & Gunn, J. E. 1991, AJ, 101, 2004
Schneider, D. P., et al. 1993, ApJS, 87, 45
Spinrad, H., et al. 1993 AJ, 106, 1
Steidel, C. C., & Sargent, W. L. W. 1992, ApJS, 80, 1
Stocke, J., Shull, J. M., Penton, S. V., Donahue, M., & Carilli, C. 1995, in ESO Workshop on QSO Absorption Lines, ed. G. Meylan (Berlin: Springer), 347
Treyer, M. A., & Silk, J. 1994, ApJ, 436, 143
Tytler, D., Fan, X.-M., Burles, S., Cottrell, L., Davis, C., Kirkman, T., & Zuo, L. 1995, in ESO Workshop on QSO Absorption Lines, ed. G. Meylan (Berlin: Springer), 289
Wampler, E. J. 1986, A&A, 161, 223
Weymann, R. J. 1993, in The Environment and Evolution of Galaxies, ed. J. M. Shull & H. A. Thronson (Dordrecht: Kluwer), 213
Weymann, R. J., Carswell, R. J., & Smith, M. G. 1981, ARA&A, 19, 41
Wyse, R. F. G. 1993, in The Environment and Evolution of Galaxies, ed. J. M. Shull & H. A. Thronson (Dordrecht: Kluwer), 305
Young, P. J., Sargent, W. L. W., & Boksenberg, A. 1982, ApJS, 48, 455